Analysis of Crack Propagation Transients in Accelerated Fatigue Characterization of Adhesives

Carlos G Dávila[1] and Cheryl A. Rose[1]

[1] NASA Langley Research Center, Hampton VA 23692, USA

Abstract. Fatigue analyses of adhesively bonded composite laminates were conducted to investigate discrepancies in experimentally measured rates of crack propagation in double cantilever beam specimens subjected to increasing or decreasing load histories. A cohesive fatigue damage model that accounts for the quasi-static traction-separation response and bridging was used in a finite element model of the test to identify transient effects caused by the evolution of the process zone in the adhesive, as well as the long-range, low-intensity bridging induced by the knit supporting carrier inside the adhesive. In addition to the quasi-static cohesive properties, the fatigue model requires two parameters that were obtained by fitting the rates of propagation at two experimental data points. The results indicate that the analyses accurately reproduce transient and steady-state rates of propagation observed in the experimental results, as well as the threshold of propagation. Transient rates of propagation consistently exceed those in steady state, which underscores the need to understand transients and account for them in fatigue characterization. The results also highlight that a Paris curve for steady-state propagation can be obtained most quickly using a decreasing load function, but that this curve is an unconservative bound to the rates of propagation. A lateral shift in the Paris curve is proposed for a conservative characterization that removes the effect of bridging and other R-curve effects.

Keywords: Cohesive Elements, Fatigue Analysis, Crack Propagation Rate.

1 Introduction

Adhesively bonded joints possess several advantages compared to mechanical fastening, especially in the assembly of large composite structures where they provide lower structural weight, lower manufacturing cost, and excellent fatigue resistance. However, reliable material models for the prediction of damage tolerance and residual life of adhesive joints are only beginning to emerge. In addition, efficient standardized procedures are needed to more easily and inexpensively characterize the material properties needed for these models.

Cohesive analysis has been shown to be a powerful and general tool that can predict the behavior of adhesively bonded joints in composite structures in which several damage modes interact with adhesive failure [1]. The main benefit of cohesive models is that they can reproduce localized deformation and load transfer in the vicinity of the crack tip, which linear elastic fracture mechanics (LEFM) cannot. Cohesive models provide a natural representation of the transition between damage initiation and propagation and are therefore particularly well suited for the analysis of bonded joints with modern, high-toughness, structural adhesives that exhibit large process zones.

In a fatigue loading regime, a structure may fail at a load much smaller than the static strength. Therefore, fatigue analysis and residual strength prediction are needed, especially in the cases of fail-safe or damage tolerant designs. However, accurate prediction of fatigue life is a challenge due to the complicated nature of fatigue crack initiation and propagation, the effects of the configuration of the bonded joints, the complex material behavior under different stress ratios and mode mixities, and the effort required to perform experimental characterization of adhesive fatigue.

A complete characterization of the rate of crack propagation must cover an extensive range of driving forces, from threshold to critical crack growth rate regimes (J_{th} to J_c). To sweep this range, fatigue fracture characterization tests are usually conducted under either force or displacement control. In a double cantilever beam (DCB) subjected to force control (FC), the maximum applied load remains constant while the corresponding opening displacement and peak crack driving force, J^{max}, gradually increase with crack length. Therefore, FC is the preferred method for reaching the high end of the propagation range. Conversely, the propagation rate under displacement control (DC) slows down as the crack extends, so DC is useful for reaching the threshold of propagation, J_{th}. The work of Weeks and Czabaj [2] aims at the standardization of the procedures to characterize the static and fatigue crack propagation in adhesively bonded composites. The effort includes the characterization of the mode I traction-separation law (TSL) of the AF163-2K film adhesive, as well as the exploration of a protocol for accelerated J-controlled fatigue testing. Several load control histories were evaluated, including constant J^{max}, increasing J^{max}, and decreasing J^{max}. An unexpected discrepancy was observed in values of the rates of propagation obtained from increasing and decreasing J^{max} tests. The cause for this discrepancy could not be ascertained, and this experimental observation motivated the analyses presented herein.

The analysis of fatigue can be classified into three categories that are often considered independently: fatigue strength and lifetime prediction, fatigue crack initiation, and fatigue crack propagation. However, progress has recently been made in the development of holistic models that capture all aspects of fatigue damage. Allegri [3]identified intrinsic relationships between stress-based life response, crack onset, and the rate of crack propagation. The CF22 cohesive fatigue model [4] takes advantage of these intrinsic relationships to predict rates of propagation using stress-life (S-N) diagrams and engineering assumptions such as the Goodman Diagram. Therefore, the S-N-based CF22 cohesive model is ideally suited to investigate the discrepancies observed in the rates of propagation measured with different load control functions, where long-range, low-stress bridging can induce transient effects on the crack propagation rates.

The main objective of the present effort is to perform a detailed analysis of the experimental data in [2] to aid in identifying potential sources of discrepancies in the experimental results and help guide the standardization of fatigue test protocols for adhesively bonded interfaces and delamination. The next section starts with a concise description of the mode I capabilities of CF22 and the effects of the model parameters on the predicted fatigue damage. Next, the basic aspects of the experimental campaign in [2] for the characterization of fatigue crack growth in an adhesive bond by a J-integral method are summarized. Then, the finite element model used herein and the methodology to determine the fatigue parameters for input to the CF22 model are described. Finally, the experimental and analysis results of tests performed to characterize the fatigue performance of AF163-2K film adhesive are presented. A discussion on a conservative characterization of the fatigue data for adhesives and interfaces with long-range bridging by means of a shifted Paris curve completes this effort.

2 CF22 Cohesive Fatigue Model

The CF22 cohesive fatigue damage model predicts the accumulation of damage sustained by cyclic loading inside an envelope outlined by a bilinear cohesive law as shown in Fig. 1. The critical displacement jumps, $\varDelta_c$ and $\varDelta_f$, the initial stiffness, K, and the strength, σ_c, of the cohesive envelope are shown in this figure. Since any point outside of the cohesive outline corresponds to a failed material state, the outline represents the envelope of the damage process. Damage at a point *P* accumulates with the number of cycles at a rate that depends on the relative displacement jump, λ/λ^*.

The CF22 fatigue damage accumulation function proposed in [4] has the form:

$$\frac{dD}{dN} = \frac{1}{\gamma}\frac{(1-D)^{-q}}{E^{\beta}(\beta+q+1)}\left(\frac{\lambda}{\lambda^*}\right)^{\beta} \tag{1}$$

where q is a model parameter, and *D* is an energy-proportional damage norm defined as:

$$D = \frac{\lambda-\varDelta_c}{\varDelta_f-\varDelta_c} \tag{2}$$

and where the relative endurance, *E,* is the stress severity below which fatigue damage does not accumulate: $E = S_{no\_fat} = \sigma_{no\_fat}^{max}/\sigma_c$. The term γ in Eq. 1 is the number of cycles to endurance, which is set to $\gamma = 10^6$ cycles [5]. The damage accumulation function given by Eq. 1 is designed to reproduce an idealized S-N curve that has the following slope:

$$\beta = \frac{-\eta\log\gamma}{\log E} = \frac{-6\eta}{\log E} \tag{3}$$

where $\eta \approx 1$ is an optional "brittleness" parameter that can be used to represent the low-cycle plateau in an S-N curve. In mode I, the endurance as a function of stress ratio, *R*, can be estimated from the Goodman Diagram, which gives [4]:

$$E = \frac{2\varepsilon}{\varepsilon+1+(\varepsilon-1)R} \tag{4}$$

The parameter ε in Eq. 4 is the relative endurance limit for full stress reversal: $\varepsilon = E(R=-1)$.

In summary, the parameters of the fatigue model are η, ε, and q. The procedure to calculate fatigue damage using a material subroutine for cohesive elements consists of calculating E using Eq. 4, the S-N exponent β with Eq. 3, and then the rate of damage accumulation with Eq. 1. It was shown in [4] that, when used in a finite element model, this model can predict a Paris-type crack propagation curve of the form:

$$\frac{da}{dN} = C\ (J^{max})^m \tag{5}$$

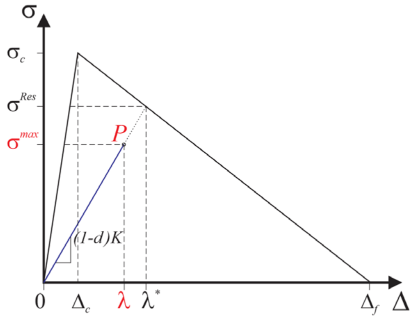

Fig. 1. Cohesive law with fatigue damage: definition of displacement jumps in fatigue.

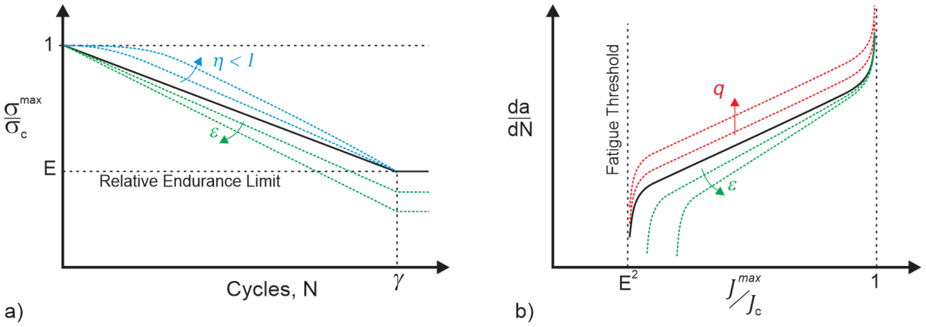

Fig. 2. Effect of CF22 model parameters η, ε, and q on: a) S-N diagram; b) propagation rates.

The effect of the three model parameters is illustrated in Fig. 2, where it can be observed that η can be used to represent a low-cycle plateau in the S-N curve, ε affects the slope of both S-N and Paris crack propagation curves, and q shifts the Paris curves up or down, but it does not affect the S-N curves.

The CF22 cohesive fatigue model was developed using a bilinear cohesive law. Quasi-static and fatigue R-curve effects can be represented by superposing two or more bilinear cohesive laws [6]. The procedure consists of replicating the layer of cohesive elements while keeping the element connectivities unchanged. The properties of each layer of bilinear cohesive elements are chosen such that the sum of the contributions of all layers produces the multi-linear shape of the TSL of interest. The main advantage of superposing bilinear elements as opposed to constructing a single multilinear TSL is that thermodynamically consistent multilinear cohesive laws capable of mode mixity are difficult to formulate [7], while most bilinear laws do have this capability. The method of superposition has been demonstrated among others in quasi-static and fatigue analyses of delamination with fiber bridging [5], in a specimen for skin/stiffener separation [4], and will be used in Section 4 to represent the TSL of an adhesive bondline.

3 Experimental Procedure for the Characterization of 3M AF163-2K Film Adhesive

The adhesive characterization tests described in this section were performed as part of an effort to develop standardized procedures for characterizing the fatigue and fracture response of adhesives [2]. The effort consists of a quasi-static characterization of the TSL in adhesively bonded DCB specimens, followed by a characterization of the rates of crack propagation in DCB specimens subjected to J-controlled cyclic loading. The specimen adherends were made of Hexcel IM7/8552 carbon/epoxy tape prepreg with a stacking sequence of $[0_{18}]$ with a nominal total thickness of 3.48 mm. To prepare for adhesion, one surface of each composite panel was grit blasted and then wiped using acetone to clean the surface. The adherends were secondarily bonded with 3M AF163-2K film adhesive and cured in an autoclave. 3M AF163-2K is a tough epoxy film adhesive with a knit carrier [8]. This embedded carrier is designed for a bondline thickness of 0.24 mm, which was further controlled by placing 0.229-mm steel wires on the adhesive film around the circumference of the panels. A 50.8-mm starter crack was created using a 12.5-µm-thick Teflon film insert. The panels were cut into specimens of three different widths, b = 25 mm, 10 mm, and 5 mm, for an investigation of the effect of specimen width and anticlastic bending on the characterization of the TSL as discussed in [2]. Since the anticlastic bending effects and crack-front curvature are minimized in the narrower specimens (b = 5 mm), TSLs derived from these specimens are assumed, for the purposes of this study, to provide results that are most representative of the true adhesive response.

The TSL was obtained from the J-integral:

$$J_I = \frac{2P}{b} sin\theta \tag{6}$$

where P is the applied load. In the quasi-static test, the rotation of the arms under the load application point, θ, was measured using digital image correlation (DIC). In addition, a stationary camera positioned towards the initial crack tip was used to measure the crack opening displacement jump, δ_n. The TSL was obtained by differentiation of the J-integral:

$$\sigma(\delta_n) = \frac{dJ_I}{d\delta_n} \tag{7}$$

Fatigue testing for the characterization of the rate of propagation, da/dN, was conducted in J-control, i.e., the applied force is controlled to ensure that J^{max} follows a specified function of the cycle count. The main benefit of this method is that loading functions can be designed such that the entire range of the Paris curve can be swept with a single specimen and using a limited number of load cycles. During a fatigue test, DIC cannot be used to provide continuous data to the load actuator, so inclinometers connected to the load actuator were used to measure rotations. The crack length was measured every 1,000 cycles for a total of 20,000 cycles or up to the point when the maximum displacement reached the limits of the machine. All tests were conducted at a stress ratio of $R = 0.55$ and at a frequency of 0.5 Hz. This relatively large stress ratio and low frequency were selected to reduce the effects of acceleration on the inclinometers. To reduce anticlastic bending and the curvature of the propagation front, the fatigue tests were conducted using relatively narrow specimens with a nominal width of 10 mm.

The fatigue characterization of the adhesive is performed by plotting the rates of crack propagation in terms of J^{max}. Although J-controlled loading can potentially allow a faster characterization of adhesive fatigue, the experimental results indicate that different rates of propagation are obtained from increasing and decreasing J-controlled tests. The reason for this inconsistency was not identified, and this observation became the main motivation for the present modeling effort. In the next section, analyses are performed to resolve the cause of this discrepancy.

4 Finite Element Analyses of Adhesive DCB Test

The two-dimensional model of the DCB specimens shown in Fig. 3 was constructed in Abaqus. Each arm of the model is composed of six layers of CPE4 plane strain elements with the material properties shown in Table 1. The length of the refined propagation region of the model is 110 mm long, and the elements in this region are 0.2 mm long. The adhesive was represented using 0.24-mm-thick COH2D4 cohesive elements.

The mode I TSL of an adhesive can be represented using a multilinear cohesive element. However, most multilinear cohesive laws do not ensure thermodynamic consistency in mixed mode [7] while bilinear cohesive formulations are intended for mixed-mode analyses. To ensure that the procedure proposed here is compatible with mixed-mode fracture problems, a method based on the superposition of bilinear laws developed by the authors was used [6]. The procedure consists of duplicating the layer of cohesive elements while keeping the element connectivities unchanged. The properties of these two embedded layers of elements, referred to as A and B, were chosen such that the sum of the two laws fits the experimental TSL, as shown in Fig. 4. The initial stiffness of law B is calculated to ensure that damage in law B starts at the final opening displacement of law A $\left(\Delta_f^A = \Delta_c^B\right)$, so damage progresses continuously between laws A and B. The energy release rate (ERR) of cohesive laws A and B combined is $J_c^{TSL} = 2.992$ N/mm, which corresponds to the area under the experimental TSL. A closer fit of the shape of the "tail" of the experimental TSL could be achieved by using three or more superposed cohesive laws, but the effects of such adjustments disappear after the opening displacements exceed 0.2 mm. Therefore, there is no benefit in performing exact fits of the shape of a TSL when conducting analyses of crack propagation when the opening displacements far exceed those of the TSL. The cohesive properties of laws A and B are shown in Table 2. This table also reports the cohesive properties of the adhesive knit carrier, which is described in the next section.

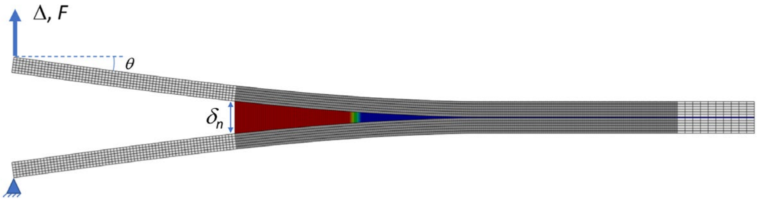

Fig. 3. Two-dimensional cohesive model of adhesively bonded DCB specimen.

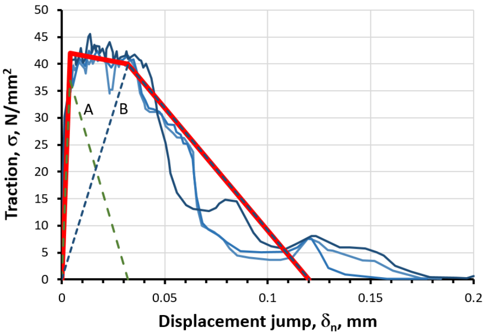

Fig. 4. TSL extracted from three quasi-static tests of narrow DCB specimens (blue) and trilinear cohesive law (red) resulting from the superposition of bilinear laws A and B (green dashed lines). Specimen width is 5 mm.

Table 1. Material properties of IM7/8552 [9].

E11 (avg T/C) (MPa)	E22=E33 (MPa)	G12=G13 (MPa)	G23 (MPa)	ν12=ν13	ν23
146,700.	8700.	5160.	3000.	0.32	0.4

Table 2. Cohesive properties of AF163-2K film adhesive.

Cohesive Law	K (N/mm^3)	J_c (N/mm)	σ_c (MPa)
A	9250.	0.592	37.
B	1250.	2.4	40.
Carrier bridge	0.05	0.24	0.1

4.1 Quasi-Static Analyses of Adhesively Bonded DCB Specimens

The quasi-static response of the 5-mm-wide DCB specimens predicted using the superposition of cohesive laws A and B is shown as a dashed red line in Fig. 5a. This predicted response fits the average of the experimental data (three blue curves), up until a load-point displacement of about 10 mm. Then, the predicted response falls slightly below the average of the experimental curves. The J versus crack tip opening plot shown in Fig. 5b confirms that the TSL induces a rapid rise in J, followed by a plateau that does not capture the remaining rise in J.

At a load-point displacement equal to 12 mm, the red dashed curves start to deviate from the experimental results. At this point, the opening displacement at the location of the initial crack tip is approximately 2 mm, which is more than ten times larger than the final opening displacement of the TSLs shown in Fig. 4 (0.15 – 0.18 mm). This difference in scale indicates that the measured TSL lacks a contribution from a low-stress, long-range toughening mechanism. This long-range mechanism, which contributes to the fracture response well after the TSL is exhausted, is bridging. Bridging in the AF163-2K adhesive starts as a diamond-shaped net that connects the arms in the wake of the crack tip, and it evolves into a chaotic field of broken and unbroken strands, as can be observed in Fig. 6. Other studies of the fracture of AF163-2K adhesive confirm that the bridge of knit carrier induces an R-curve increase in the adhesive's resistance to crack propagation [10].

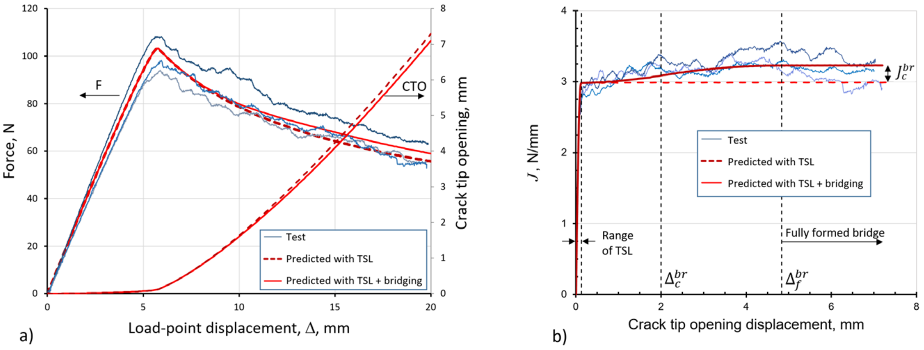

Fig. 5. Experimental and predicted DCB test: a) force-displacement response and crack tip opening, b) J versus crack tip opening. Specimen width is 5 mm.

To represent the effect of bridging on the response, a third cohesive law was superposed with the TSL. The critical ERR for this bridging law, J_c^{br}, corresponds to the rise in the resistance curve (Fig. 5b). The remaining properties of the bridging law were determined by fitting the average force-displacement response in the range of load-point displacements between 12 mm and 16 mm (opening displacements of 2 mm and 4.8 mm, respectively, Fig. 5a – right ordinate axis). The bridging strength, σ_c^{br}, was set to achieve complete failure of the bridging at a crack tip opening displacement of $\Delta_f^{br} = 2J_c^{br}\sigma_c^{br}$ = 4.8 mm. The bridging stiffness, K, was calculated somewhat arbitrarily such that softening initiates at an opening displacement of $\Delta_c^{br} = \sigma_c^{br}/K$ = 2 mm. The resulting properties for the knit carrier bridging are shown in Table 2. With bridging included, the critical ERR of the adhesive, J_c^{adh}, is equal the sum of the ERRs of the three cohesive laws, or 3.23 N/mm. The response and resistance curve of the model with all three superposed cohesive properties are shown as solid red curves in Figs. 5a and 5b, respectively. It can be observed that the effect of bridging on the quasi-static response of the adhesive is small, as expected of a cohesive law with a bridging strength and fracture toughness that are 0.5% and 8% of the strength and toughness of the adhesive, respectively. However, it will be shown that this small bridging contribution is the cause of the apparent discrepancies observed in the experimental rates of fatigue crack propagation.

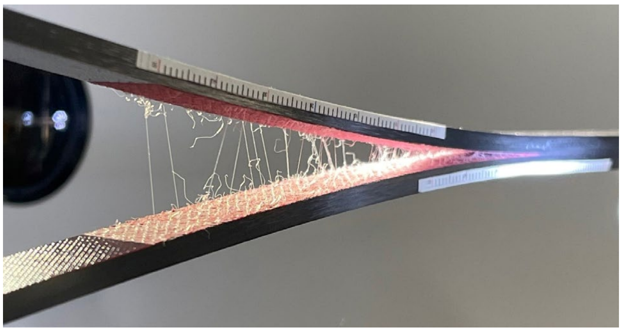

Fig. 6. Bridging of the cracked faces due to the embedded adhesive knit carrier.

An examination of the predicted quasi-static process zones for each of the cohesive laws used to represent the adhesive response indicates that the cohesive zone length for law A is 1.3 mm. The cohesive law B is designed such that it begins to soften immediately after law A is exhausted and it measures 2.3 mm. Therefore, the combined length of the cohesive zone of the TSL, which represents the entire process zone of the adhesive, is 3.6-mm long. The effect of bridging starts at the leading crack tip and builds up gradually. Damage of the bridging law starts about 25 mm behind the leading crack tip and ends 43 mm behind the tip. It was observed that once these process zones have formed, their lengths remain constant as they follow in the wake of the leading crack tip.

4.2 Simplified Cyclic Loading (SCL) Procedure and the Simulation of J-Controlled Fatigue

Fatigue analyses were conducted using the DCB model described earlier with a simplified cyclic loading (SCL) procedure. The SCL procedure consists of two steps, in which the first step consists of a quasi-static ramp representing the first load cycle and is followed by a second step representing the cyclic loading. During the second step, the maximum load is applied without cycling – the constitutive model accounts for the cyclic nature of the load based on the value of the stress ratio, R, supplied to the CF22 subroutine. The cycle count is approximated as a real number equal to the pseudo-time of the analysis. When the severity approaches $\mathrm{S} = 1$, the analysis time increment can be a small fraction of a cycle, but when the severity approaches the endurance, the time increment can increase to any high cycle jump specified by the analyst in the analysis solution card.

To simulate J-controlled loading, a user-written amplitude (UAMP) subroutine was developed. The subroutine uses three sensors: the reaction force at the load application point, F_z^P; the displacement at the load application point, u_z^P; and the displacement of the adjacent point, u_z^{P+1}. At every analysis increment, a term is calculated that, for small to moderate rotations, is proportional to the J-integral (Eq. 6):

$$J_{constant} = \| F_z^P (u_z^{P+1} - u_z^P) \| \tag{8}$$

During the first step of the analysis, which corresponds to the half cycle, the maximum load is ramped up and $J_{constant}$ increases with the applied load. When the second step begins, fatigue damage is enabled and $J_{constant}$ is held at the value calculated at the end of the first step. Then, the amplitude of the applied load is recalculated as at every increment:

$$\text{ampValueNew} = \text{ampValueOld} * \sqrt{\frac{A(N) \cdot J_{constant}}{\| F_z^P (u_z^{P+1} - u_z^P) \|}} \tag{9}$$

where the term ampValueOld is the load amplitude of the previous increment, which is provided by Abaqus as an input to the subroutine. The function $A(\text{N})$ is a scaling factor. For a constant J^{max} loading condition, $A(\text{N}) = 1$. For a linearly increasing or decreasing J^{max}, $A(\text{N})$ is defined as a function of cycle count, N, the ratio of the final over the initial J^{max}, Γ, and the desired final number of cycles, N_{final}:

$$A(\text{N}) = N \frac{\Gamma - 1}{N_{final}} + 1, \quad \text{where} \quad \Gamma = \frac{J_{final}^{max}}{J_{initial}^{max}} \tag{10}$$

Analyses were conducted by subjecting the DCB model to the five experimental cases reported in [2]. These cases consist of three cases where J^{max} is constant (Hi, Mid, Lo), one in which it increases in steps (Inc), and one in which it decreases in steps (Dec). The J^{max} for the analysis was calculated using Eq. 6 and the rotations of the arms of the finite element model. The results shown in Fig. 7 demonstrate that the analyses (solid lines) approximate the experimental loading histories (dashed lines).

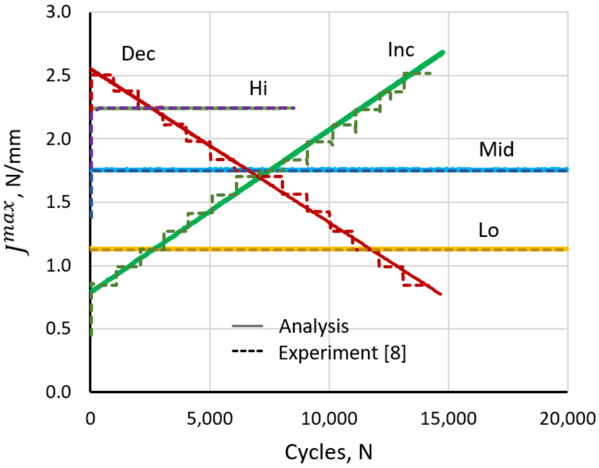

Fig. 7. J-control loading histories – experiment and analysis.

4.3 Identification of Fatigue Model Parameters

One of the main benefits of the CF22 cohesive fatigue model is that it requires few parameters, all of which are easily identifiable. For a mode I problem, the parameters are η, ε, and q. The first parameter, η, is optional, and it is mostly useful to reproduce low-cycle plateaus in stress-life (S-N) diagrams. Since this effect is not of particular concern here and no experimental S-N data is available, the default value of $\eta = 0.95$ was used [5]. The parameters ε and q were determined by trial and error by matching the steady-state rates of propagation for the two J-constant load cases referred to as "Lo" and "Hi". These points correspond to J_{Lo}^{max}=1.13 N/mm and J_{Hi}^{max}=2.25 N/mm, and the steady-state rates of propagation are $1.8{\cdot}10^{-4}$ mm/cycle and $1.0{\cdot}10^{-1}$ mm/cycle, respectively. As in previous work, the same ε and q fatigue model parameters were applied to the A and the B cohesive laws. This iterative procedure for parameter identification is quick, as it can be conducted in about six iterations. However, more rigorous approaches have been proposed [11].

The fatigue parameters for the knit carrier bridging are not necessarily the same as those used for the TSL, which renders their calibration more difficult. Therefore, the effect of the bridging on fatigue was evaluated by performing analyses using three models that bound the response. In the first model, the base TSL composed of laws A and B is considered in the simulation, but bridging is not. In the second model, a bridging law is added, and the same fatigue model parameters ε and q are applied to all three cohesive laws. In the third model, all three cohesive laws are used, but the fatigue damage accumulation in the bridging law is disabled, i.e., bridging is assumed to respond as a nonlinear spring subject to quasi-static damage and not subjected to additional fatigue damage. These three models are referred to as TSL, TSL+Bridge, and TSL+BridgeNF. For each model, the fatigue parameters, ε and q, shown in Table 3, were determined by trial and error as described above.

Table 3. CF22 Fatigue Model Parameters for the three models evaluated.

	TSL	TSL+Bridge	TSL+BridgeNF
ε	0.10	0.12	0.13
q	−0.6	1.0	1.4

The results of the three models for increasing (Inc) and decreasing (Dec) loading histories are shown in Fig. 9. All three models exhibit similar characteristics and rates of propagation. The Inc propagation rates (green curves) start by decreasing before they increase. This initial decrease corresponds to the formation of the process zone in the adhesive during the first loading cycles. When the TSL at the initial crack tip reaches final separation (d =1), the rate of propagation starts a steady-state increase along a line corresponding to a Paris law. This starting point is labeled SS in each of Figs. 8 a–c. In addition, the two models that include bridging exhibit a second steady-state point, SS2, where the bridge reaches final separation at the initial crack tip (Figs. 8 b, c).

The predicted rates of propagation for the Dec loading cases (red curves in Fig. 8) also start with a rapid decrease in the rate of propagation due to the formation of the adhesive process zone. These curves also exhibit steady-state initiation points, but, due to the high loads, they occur within a few cycles and are not easily discernible. Then, the rates of propagation begin steady-state propagation along straight Paris lines, until they begin to curve at the low end of the loading range, where the applied J^{max} approaches the threshold of propagation. Although the rates predicted by the three models are similar, one feature distinguishes them: the separation between the Inc and Dec curves between the points SS and SS2. This separation would not occur without the long-range toughening induced by the bridging law. It will be shown in the next section (see Fig. 10) that the experimental data exhibits a clear separation between the two loading cases. Since the experimental data was not reproduced with either the TSL nor the TSL+Bridge models, these models were discarded. In the remainder of this paper, the TSL+BridgeNF model is retained.

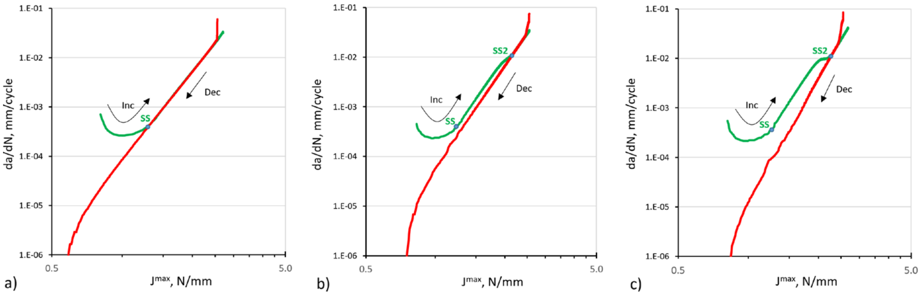

Fig. 8. Propagation rates for increasing and decreasing loading histories: a) TSL model; b) TSL+Bridge model; c) TSL+BridgeNF model.

4.4 Results of Fatigue Analyses of Adhesively Bonded DCB Specimens

The analysis results for the five loading cases are shown as solid curves in Fig. 9. The experiment consists of data from nine test specimens consisting of two tests conducted in Inc loading, two tests conducted in Dec loading, and five tests conducted in constant loading, three in Mid, one in Hi, and one in Lo. The experimental data is plotted as symbols with different shades of the same color representing different test specimens subjected to the same loading function. The experimental rates of propagation were originally calculated every 1000 cycles using backward differentiation from visual measurements of the crack length [2]. For example, the first experimental data point at 1000 cycles consists of the quasi-static process zone length (lpz) from the initial load application plus any fatigue damage accumulation for the remaining 999 cycles. A more accurate representation of these experimental rates was obtained by shifting the data by 500 cycles to the center of the differentiation interval. It can be observed that the predicted steady-state rates of propagation for J_{Lo}^{max} (Lo) and J_{Hi}^{max} (Hi) correlate very well with the experimental data, which is to be expected since the model parameters ε and q were determined by matching these two rates. The predictions made with these two parameters correlated well with test data from all other load cases.

The fatigue characterization of the adhesive is performed by plotting the rates of crack propagation in terms of J^{max}, as shown in Fig. 10. The experimental data confirms that the rates of propagation for Dec loading and Inc loading diverge over most of the loading range. The reason for this difference is that, for any point in the range 1 N/mm < J^{max} < 2 N/mm, the lpz for Dec loading is much longer than that for Inc. In Dec loading, the longer crack leaves a full bridging zone in its wake, while in Inc loading the length of propagation is too short to benefit from the shielding provided by a fully formed bridging zone. Since crack propagation for Dec loading is in a steady-state condition for most of the test, it can be fitted by a Paris law, as shown in Fig. 10 with a dashed line and its associated equation.

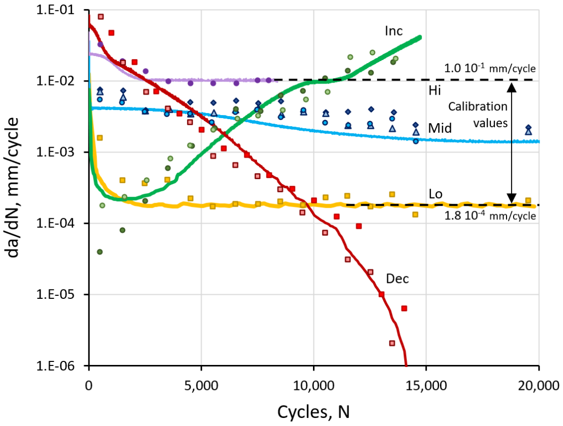

Fig. 9. Predicted and experimental rates of propagation for five loading cases considered as a function of loading cycles. The solid lines correspond to analysis results and the symbols represent experimental data.

The middle of the range of the Inc data also exhibits steady-state propagation, which starts after the process zone of the TSL is formed and gradually ends with the formation of the knit carrier bridge at $J^{max} \approx 2$ N/mm. This intermediate steady-state range can also be fitted with a Paris law. Alternatively, a fit over this range can be obtained by shifting the Paris equation for Dec loading by the contribution of the bridging law, which is $J_c^{br} = 0.24$ N/mm. It can be observed that this shifted curve represents an upper bound to the rates of propagation, except for the initial transient. Since the initial transient only applies to the formation of the process zone and is not accompanied by a crack opening, the shifted curve ensures conservative predictions when using analysis methods based on the Paris equation. In adhesives and interfaces that do not exhibit long-range bridging, increasing- and decreasing-rate curves overlap, and a conservative characterization of the adhesive does not require shifting the Paris curve.

The simulations for the three $J^{max} = constant$ load cases are labelled as Hi, Mid, and Lo in Fig. 10. The rates of propagation for these three cases start high and progressively slow down as the process zone of the TSL and the bridging form. The Hi and Mid cases reach steady state with full bridging before the end of the test at 20,000 cycles. Therefore, their rates of propagation stabilize and end on the Dec curve. The loading for the Lo case is insufficient to achieve a full bridging within 20,000 cycles, so its final propagation rate is approximately five times higher than the corresponding point on the

Dec load curve. This difference is labeled as “Gap” in Fig. 10. According to the analysis, it would take almost a million cycles and 40 mm of additional propagation for the Lo rates to reach the rate of steady-state propagation described by the Dec line.

The threshold of propagation occurs when the stresses in the process zone fall below the endurance (Eq. 4). The threshold was predicted from analysis of the Dec loading, where the analysis results indicate that crack propagation stops when $J_{th}^{adh\_fem} = 0.82$ N/mm.

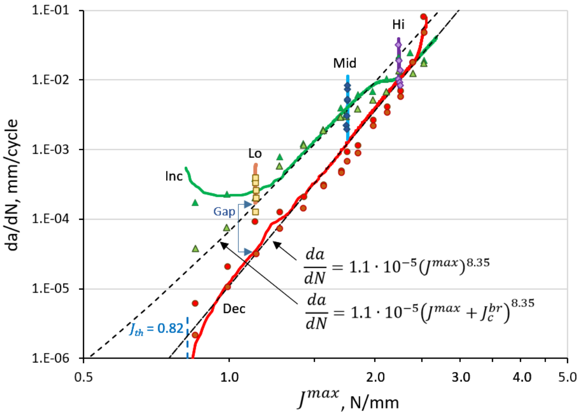

Fig. 10. Predicted and experimental rates of propagation for five loading functions of J^{max}. The solid lines correspond to analysis results and the symbols represent experimental data.

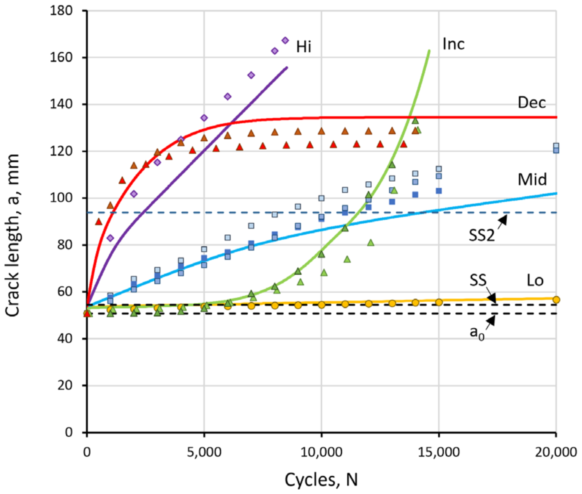

Fig. 11. Predicted and experimental crack lengths for all five loading histories considered in [2].

The primary interest in performing fatigue propagation analyses is to determine the crack length after a certain number of load cycles. The predicted crack lengths for the five loading histories considered here are shown in Fig. 11. Dashed lines indicate the initial crack length (a_0 = 50.8 mm), the length at which the TSL is fully formed (SS), and the length at which the bridging is fully formed (SS2). It can be observed that the crack lengths for the Dec, Hi, and Mid load cases reach SS in a few cycles, while the Inc and Lo cases take about 5000 cycles to reach that point. All simulations except Lo reach SS2 before the end of the test. This plot also illustrates the effects that crack lengths have on the rates of propagation. For instance, the driving forces for Dec and Inc tests reach equal values of J^{max} =1.7 N/mm at 7080 cycles (Fig. 6). At this number of cycles, the crack extensions for these two loading cases are 80 mm and 6 mm, respectively (Fig. 11). In the case of Dec, bridging has progressed significantly past the initial crack tip and the propagation rate is in steady state, while in Inc bridging is still forming. This difference in crack extension causes a rate of propagation for Dec that is four times slower compared to Inc.

5 Concluding Remarks

The results of an adhesive fatigue characterization campaign based on different loading histories reveal that the rates of crack propagation are subject to different transient conditions. The first transient effect is a result of the formation of the process zone in the adhesive. This transient starts quasi-statically with the first ramping up of the load and may take many cycles to complete, especially when $J^{max} \ll J_c$. Until then, the stress concentration at the leading crack tip ($D \approx 0$) remains higher than at steady state and the rate of propagation is consequently also higher. For the 3M AF163-2K adhesive, when the lpz reaches about 2 or 3 mm, the process zone is fully formed, and the adhesive begins to open. Then, the lpz of the adhesive stays constant and propagation continues at steady state. A second transient that affects adhesives is induced by bridging of the carrier. The effects of this transient are much less discernable because bridging strength is several orders of magnitude smaller than the strength of the adhesive. According to the present analysis results, the process zone for bridging is 40 to 50 mm long, so it can cause discrepancies in the rates of crack propagation between tests in which the crack extensions are widely different.

The concept of characterization of the rates of propagation by means of a Paris law expressed in terms of a similitude parameter such as J^{max} or ΔJ is intended for steady-state propagation. In the presence of evolving process zones and bridging, the rates of propagation are driven by J^{max} and the stress ratio, but they also depend on the length of propagation: cracks without fully formed process zones propagate more quickly than steady-state cracks. For this reason, the experimental results under decreasing J^{max} reach steady-state more quickly: in just over 1000 cycles the crack length propagates by more than 40 mm and consumes all the bridging zone, after which propagation continues at a steady-state rate described by a Paris equation. However, steady state represents an unconservative lower bound of the rates of propagation. An upper bound of the propagation rate consists of the quasi-static growth of the crack tip during the first load application, which is an impractically high rate that only applies to the initial cycle and is not accompanied by opening of the crack (damage $\approx$ 1). A more practical upper bound could be obtained from a decreasing load test, and then shifting the Paris curve by the critical energy release rate of the bridging, which is 0.24 N/mm for the adhesive examined herein. Considering that the initial transient occurs before the adhesive opens, using such a shifted curve ensures a conservative prediction of crack propagation. This approach is useful for characterizing adhesives and interfaces in which R-curve effects induce discrepancies between the propagation rates measured for different loading histories.

The accuracy of the predictions and the ease with which the model parameters are obtained also demonstrate the potential of this methodology as a tool for the design of damage-tolerant joints with specified inspection intervals. However, the application of this methodology to general composite laminates and loading conditions may have to account for additional challenges, such as the effect of mode mixity, different stress ratios, the migration of the crack into the laminate, residual thermal stresses, load spectra, material variability, and more.

References

1. Leone, F.A., Dávila, C.G., Girolamo, D.: Progressive damage analysis as a design tool for composite bonded joints. Composites Part B: Engineering. 77, 474–483 (2015).
2. Weeks, S., Czabaj, M.: Static and Fatigue Characterization of Mode I Fracture in Adhesively Bonded Composites Based on the J-Integral Approach. In: American Society for Composites 2023. Destech Publications, Inc. (2023)
3. Allegri, G.: Modelling fatigue delamination growth in fibre-reinforced composites: Power-law equations or artificial neural networks? Mater. Des. 155, 59–70 (2018).
4. Dávila, C.G., Rose, C.A., Murri, G.B., Jackson, W.C., Johnston, W.M.: Evaluation of Fatigue Damage Accumulation Functions for Delamination Initiation and Propagation. Technical Publication NASA/TP–2020-220584. (2020). https://ntrs.nasa.gov/citations/20200003113
5. Dávila, C.G., Joosten, M.W.: A cohesive fatigue model for composite delamination based on a new material characterization procedure for the Paris law. Engineering Fracture Mechanics. 284, 109232 (2023). https://doi.org/10.1016/j.engfracmech.2023.109232
6. Dávila, C.G., Rose, C.A., Camanho, P.P.: A procedure for superposing linear cohesive laws to represent multiple damage mechanisms in the fracture of composites. Int. J. Fracture. 158, 211–223 (2009).
7. De Carvalho, N.V., Czabaj, M.W., Ratcliffe, J.G.: Piecewise-linear generalizable cohesive element approach for simulating mixed-mode delamination. Engineering Fracture Mechanics. 242, 107484 (2021).
8. 3M: Scotch-WeldTM Structural Adhesive Film AF 163-2 Technical Datasheet. https://www.3m.com/. (2009)
9. Wanthal, S., Schaefer, J., Justusson, B., Hyder, I., Engelstad, S., Rose, C.A.: Verification and Validation Process for Progressive Damage and Failure Analysis Methods in the NASA Advanced Composites Consortium. In: ASC 32nd Technical Conference. American Society for Composites, Purdue University, West Lafayette, IN (2017)
10. Heide-Jørgensen, S., Teixeira De Freitas, S., Budzik, M.K.: On the fracture behaviour of CFRP bonded joints under mode I loading: Effect of supporting carrier and interface contamination. Composites Science and Technology. 160, 97–110 (2018).
11. Leciñana, I., Zurbitu, J., Renart, J., Turon, A.: A robust fatigue parameter determination method for a local fatigue Cohesive Zone Model. Int. J. of Fatigue. 107582 (2023).